Going with the Flow

YOUSUF SOLIMAN, Caltech, USA and SideFX, Canada
MARCEL PADILLA, TU Berlin, Germany
OLIVER GROSS, TU Berlin, Germany
FELIX KNÖPPEL, TU Berlin, Germany
ULRICH PINKALL, TU Berlin, Germany
PETER SCHRÖDER, Caltech, USA

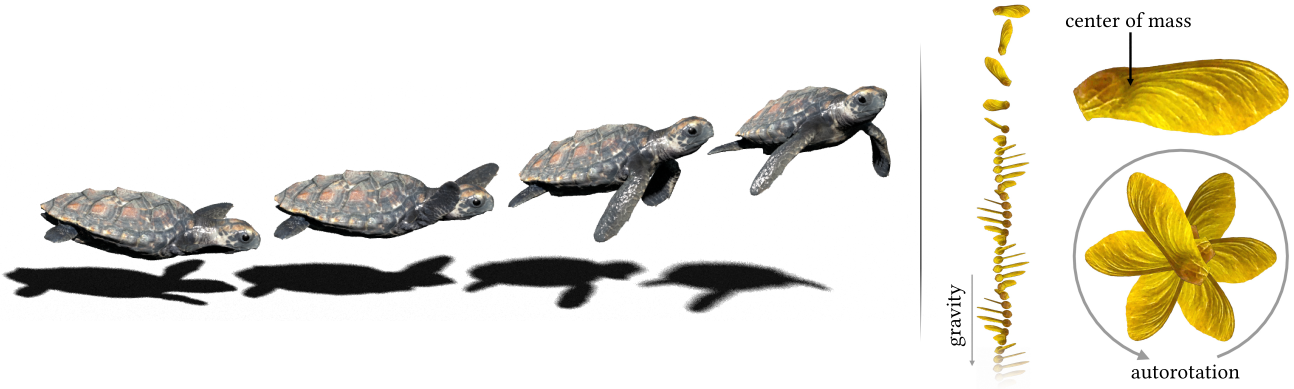

Fig. 1. Given a sequence of poses, here the swimming stroke of a turtle model, the corresponding swimming motion in water results without the need to simulate the ambient fluid (Turtle, left; see also Sec. 7.3) (Video 0:03.). Dropping a Maple seed model in air results in autorotation without the need to simulate the airflow (Maple seed, right; see also Sec. 7.2) (Video 1:15.).

Given a sequence of poses of a body we study the motion resulting when the body is immersed in a (possibly) moving, incompressible medium. With the poses given, say, by an animator, the governing second-order ordinary differential equations are those of a rigid body with time-dependent inertia acted upon by various forces. Some of these forces, like lift and drag, depend on the motion of the body in the surrounding medium. Additionally, the inertia must encode the effect of the medium through its *added mass*. We derive the corresponding dynamics equations which generalize the standard rigid body dynamics equations. All forces are based on local computations using only physical parameters such as mass density. Notably, we approximate the effect of the medium on the body through local computations avoiding any global simulation of the medium. Consequently, the system of equations we must integrate in time is only 6 dimensional (rotation and translation). Our proposed algorithm displays linear complexity and captures intricate natural phenomena that depend on body-fluid interactions.

Authors' addresses: Yousuf Soliman, Caltech, Pasadena, CA, USA and SideFX, Toronto, Canada, ysoliman@caltech.edu; Marcel Padilla, TU Berlin, Berlin, Germany, padilla@math.tu-berlin.de; Oliver Gross, TU Berlin, Berlin, Germany, ogross@math.tu-berlin.de; Felix Knöppel, TU Berlin, Berlin, Germany, knoeppel@math.tu-berlin.de; Ulrich Pinkall, TU Berlin, Berlin, Germany, pinkall@math.tu-berlin.de; Peter Schröder, Caltech, Pasadena, CA, USA, ps@caltech.edu.

0730-0301/2024/7-ART57
https://doi.org/10.1145/3658164

CCS Concepts: • **Applied computing** → **Physics**; **Engineering**; • **Computing methodologies** → **Modeling methodologies**; **Physical simulation**; **Motion processing**;

Additional Key Words and Phrases: Rigid body dynamics, shape change, lift, drag, Kirchhoff tensor, swimming

ACM Reference Format:
Yousuf Soliman, Marcel Padilla, Oliver Gross, Felix Knöppel, Ulrich Pinkall, and Peter Schröder. 2024. Going with the Flow. *ACM Trans. Graph.* 43, 4, Article 57 (July 2024), 12 pages. https://doi.org/10.1145/3658164

1 INTRODUCTION

Consider a body ("swimmer") immersed in a flow of an incompressible medium such as water and assume that a sequence of poses ("stroke") is given (see the example of the turtle in Fig. 1 and Sec. 7.3). In this setting, with the changing shape given, the movement of the body is fully described by a time-dependent Euclidean motion $g(t)$ (rotation and translation), as those are the remaining degrees of freedom. This motion is governed by a second-order ordinary differential equation. At any given time forces such as those due to gravity or lift and drag due to interaction with the surrounding medium will act on the body (see the examples of the maple seed in Fig. 1 and paper copter in Fig. 11 and Sec. 7.2). These forces result in rotational and translational acceleration in accordance with the inertia tensor of the body. In distinction to the usual setup, the inertia tensor varies with time in accordance with the given sequence of poses. Additionally, it must take into account the inertia of the surrounding medium. Consider moving a plate through water

in a pool. Pushing it in the normal direction takes considerably more force than pushing it tangentially. Since the inertia tensor mediates the relationship between force and acceleration, the stronger force needed for acceleration in the normal direction appears as an *added mass*. Originally introduced by Kirchhoff [1870], it was adapted for computer graphics applications in [Weißmann and Pinkall 2012] to model rigid body dynamics underwater. Accounting for this added mass is necessary for faithful simulations as it is responsible, for example, for the sinking motion of objects in water, the slowed descent of parachutes (Figs. 2, 8 and Sec. 7.1), and the autorotation of maple seeds (Figs. 1, 10 and Sec. 7.2).

To pursue this program and deliver a practical and efficient numerical algorithm for such settings we must first derive the equations of motion for a body with time-varying inertia. These will turn out to be a generalization of the standard rigid body dynamics equations which assume constant inertia and a vacuum. The medium enters into the dynamics through the kinetic energy imparted on it by the body and appears as added mass in the inertia tensor. Importantly it couples linear and angular momentum and one can no longer separate the linear from the rotational part of the motion as is done in standard rigid body simulation (see the propeller in Fig. 2 which starts to rotate as it sinks in water). Usually, the added mass is computed based on a global solve over the fluid domain. To avoid this costly computation we derive a novel local approximation for the added mass. The result is a fast algorithm for the motion of time-varying shapes in media such as water and air. While our treatment of the medium is necessarily approximate, we are able to faithfully reproduce effects due to time-varying inertia as well as added mass, which we demonstrate through comparison with experiments.

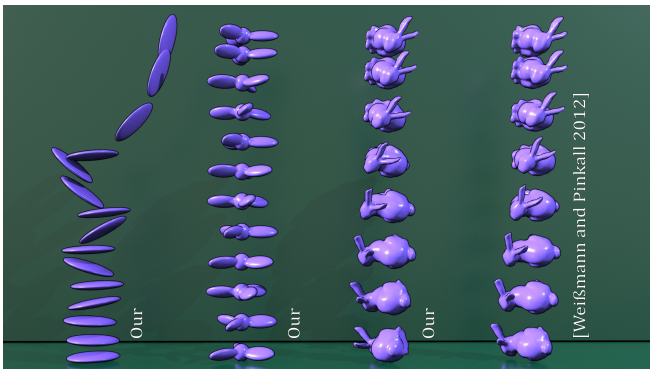

Fig. 2. Objects sinking in water exhibit motion patterns demonstrated by [Weißmann and Pinkall 2012, Figs. 1 and 2] using a costly Poisson solve for the potential field (right) while we used our local approximation (left). (Video 0:24.)

1.1 Related Work

Modeling and simulating the motion of animate and inanimate objects in fluid environments, typically water or air, has long been of interest to computer graphics researchers. Such motion can be computed through full fluid simulations [Carlson et al. 2004; Lentine et al. 2011; Tan et al. 2011], though at typically high cost. This can be avoided in low Reynolds number settings by using fractional derivatives [Ozgen et al. 2010]. More generally, local models of relevant forces such as lift and drag can be employed as was done to model swimming fish [Tu and Terzopoulos 1994; Min et al. 2019], the flight of birds [Wu and Popović 2003; Ju et al. 2013], and the floating motion of passive objects such as leaves [Wejchert and Haumann 1991]. But the fluid does not just give rise to forces acting on the immersed body. It also changes the inertia tensor through the so-called added mass [Kirchhoff 1870, 1876], reflecting the fact that any motion of the body imparts kinetic energy on the fluid. Taking account of the added mass is critical for a variety of effects such as the wobbling of coins falling in water [Heisinger et al. 2014], the rotating flight of maple seeds [Azuma and Yasuda 1989], or the motion of undulatory swimmers [Piñeirua et al. 2015]. While originally only formulated for ideal fluids, a more detailed analysis reveals the general applicability of the concept of added mass [Limacher et al. 2018] in close agreement with numerical as well as physical experiments [Limacher et al. 2019; Corkery et al. 2019]. Unfortunately even just computing the added mass for an ideal fluid, as Kirchhoff proposed, requires the solution of an integral equation over the boundary of the domain [Kanso et al. 2005; Weißmann and Pinkall 2012], which is cubic in the number of polygons but can be accelerated to linear time using a fast multipole method [Brochu et al. 2012]. Luckily we can avoid this global solve and replace it with a local computation, which we introduce. It is based on known values for primitive shapes [Brennen 2004] together with a novel account of the average mean curvature of the shape.

Our approach is inspired by, and builds on [Gross et al. 2023]. They showed that motion due to shape change can be modeled in dissipation or inertia-dominated settings with a formally identical first-order system. We give the shape-changing body in a flow its full second-order treatment. For dissipative loss we assume modest Reynolds numbers rather than small Reynolds numbers. Gross and co-workers focused on the normal/tangential anisotropy of dissipation and inertia tensors without regard to correct physical scaling while throughout we use physical parameters. Finally, in contrast to Gross and co-workers, we pull all geometry and physics back to the Lie group SE(3) of Euclidean motions where we use a variational integrator. Consequently, the resulting equations of motion are simple extensions of standard rigid body dynamics equations and so is our integrator.

2 PRELIMINARIES

The equations of motion are naturally described by the dynamics of angular and linear momenta and their change through applied forces. More formally, the dynamics are described in terms of the cotangent bundle of the group of Euclidean motions $T^*\mathrm{SE}(3)$. In this section, we briefly review some needed background and establish notation used throughout the paper.

Lie group. The state space of our body is the Lie group SE(3) of Euclidean motions in $\mathbb{R}^3$, with group multiplication given by composition. Every element $g \in \mathrm{SE}(3)$ is of the form

$$g(x) = Ax + b$$

for some $A \in \mathrm{SO}(3)$, the rotational component of the transformation, and $b \in \mathbb{R}^3$, the translational component. Using homogeneous coordinates, g can be represented as a 4×4 matrix

$$g = \begin{pmatrix} A & b \\ 0^\top & 1 \end{pmatrix}$$

so that $g(x) = g\binom{x}{1}$.

Lie algebra. Tangent vectors, *i.e.*, angular and linear velocities can be described with the aid of the Lie algebra $\mathrm{se}(3)$ which forms the tangent space of $\mathrm{SE}(3)$ at the identity. We identify it in the usual way with $\mathbb{R}^3 \times \mathbb{R}^3$—that is, a Lie algebra element is given by $Y = (\omega, v) \in \mathrm{se}(3)$ of angular and linear velocity, which can be realized as

$$Y = \begin{pmatrix} \omega\times & v \\ 0^\top & 0 \end{pmatrix}.$$

Any tangent vector $\mathring{g} \in T_g \mathrm{SE}(3)$ can be written as the pushforward of a Lie algebra element, $\mathring{g} = gY$ for some $Y \in \mathrm{se}(3)$.

In turn, angular and linear momenta are described by elements of the dual Lie algebra $\mathrm{se}(3)^*$, which we also identify with $\mathbb{R}^3 \times \mathbb{R}^3$ by using the duality pairing

$$\langle\, \mu \mid Y \,\rangle = \langle\, l,\, \omega \,\rangle + \langle\, p,\, v \,\rangle$$

where $\mu = (l, p) \in \mathrm{se}(3)^*$ and $\langle \cdot, \cdot \rangle$ denotes the standard Euclidean inner product. Note that the left slot accepts momenta (dual vectors), while the right slot is reserved for velocities (vectors).

Coadjoint action. Consider a dual Lie algebra element $\mu = (l, p) \in \mathrm{se}(3)^*$. For $g \in \mathrm{SE}(3)$, the group coadjoint action $\mathrm{Ad}^*_g \colon \mathrm{se}(3)^* \to \mathrm{se}(3)^*$ is the map defined by

$$\mathrm{Ad}^*_g \mu = (Al + b \times Ap, Ap).$$

It describes how momentum changes when one uses g to transform the frame of reference. For $Y = (\omega, v) \in \mathrm{se}(3)$, the coadjoint action is the map $\mathrm{ad}^*_Y \colon \mathrm{se}(3)^* \to \mathrm{se}(3)^*$ defined by

$$\mathrm{ad}^*_Y \mu = (l \times \omega + p \times v, p \times \omega).$$

It describes the infinitesimal change of momentum when the frame of reference changes infinitesimally by Y.

3 SETUP

We describe a shape-changing body by a time-dependent embedding

$$\gamma_t \colon B \to \mathbb{R}^3$$

where B is the compact 3-manifold with boundary over which the body is parameterized. In addition, consider an incompressible fluid, not containing the body, flowing at each time t with a certain velocity

$$\mathbf{u}_t \colon \mathbb{R}^3 \to \mathbb{R}^3.$$

When the body is immersed in the fluid at a particular location and velocity it will be subject to various forces and begin to move. With the shape of the body known, the movement of the body is described by a time-dependent Euclidean motion $t \mapsto g_t \in \mathrm{SE}(3)$. Consequently, the movement of the immersed body is given by another time-dependent embedding

$$\tilde{\gamma}_t = g_t \circ \gamma_t \tag{1}$$

of B (see, *e.g.*, [Gross et al. 2023]). The action that determines the equations of motion will be the total kinetic energy of the joint fluid-body system.

3.1 Kinetic Energy of the Body

The kinetic energy of the body is

$$E_{\text{body}} = \int_B \tfrac{1}{2} |\tilde{\gamma}'|^2 \, \rho_b \, dx,$$

where $\rho_b \colon B \to \mathbb{R}_{\geq 0}$ is the mass density of the body. Differentiating Eqn. 1 gives

$$|\tilde{\gamma}'|^2 = |\omega \times \gamma + v + \gamma'|^2,$$

where $g^{-1}g' = (\omega, v)$ is the velocity of the Euclidean motion in the body-fixed frame and γ' is the velocity of the shape-changing body sans any positioning by g. Therefore, the kinetic energy of the body defines the body inertia tensor $\mathcal{I}_{\text{body}} \colon \mathrm{se}(3) \to \mathrm{se}(3)^*$ through the equation

$$E_{\text{body}} = \tfrac{1}{2} \langle\, \mathcal{I}_{\text{body}} Y \mid Y \,\rangle + \langle\, \mu_{\text{body}} \mid Y \,\rangle + E^0_{\text{body}}. \tag{2}$$

where $Y = (\omega, v) \in \mathrm{se}(3)$, $\mu_{\text{body}} \in \mathrm{se}(3)^*$ is the momentum of γ, and

$$E^0_{\text{body}} = \int_B \tfrac{1}{2} |\gamma'|^2 \, \rho_b \, dx$$

the kinetic energy of γ without any positioning by g.

4 SIMPLIFIED FLUIDS

We now describe the simplified approach to modeling the effects of the fluid on a body. Such a body experiences lift and drag forces, which must be incorporated to generate realistic motion of, for example, leaves falling in air (Fig. 9) or objects sinking in water (Fig. 2). In addition to these forces, we also introduce a simplified model of the added mass which estimates the kinetic energy of the fluid in the vicinity of the body.

4.1 Localization of Lift and Drag

We adopt a simplified model of lift and drag forces for arbitrary bodies based on experiments with flat plates [Caplan and Gardner 2007]. The total lift and drag acting on the body is then found by summing up the local forces due to planar elements. Typically, these elements correspond to the triangles of a triangle mesh describing the boundary of the body. This yields a parameter-free model of the lift and drag forces that faithfully reproduces a variety of physical phenomena.

Lift and drag on a flat plate. Using data from an experimental study of rowing oars [Caplan and Gardner 2007] we derive an expression for the joint lift and drag force on a flat plate.

At moderate Reynolds numbers the magnitudes of the lift and drag forces F_l and F_d acting on flat plate are

$$|F_l| = \tfrac{1}{2} c_l \rho_f A |u|^2$$
$$|F_d| = \tfrac{1}{2} c_d \rho_f A |u|^2,$$

here ρ_f is the density of the fluid, A the area of the plate, u the velocity of the body relative to the fluid, and c_l and c_d are the lift and drag coefficients, respectively. These expressions have been

used successfully in the graphics literature [Tu and Terzopoulos 1994; Wu and Popović 2003; Ju et al. 2013; Min et al. 2019].

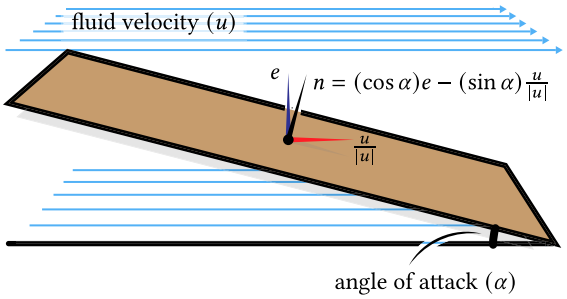

Fig. 3. Geometry of the lift and drag forces acting on a flat plate.

The crucial quantity for determining the lift and drag coefficients is the *angle of attack* $\alpha \in [0, \pi]$ defined by

$$\sin\alpha = -\langle n, \tfrac{u}{|u|}\rangle$$

where n is the unit normal to the plate. That is to say,

$$n = (\cos\alpha)e - (\sin\alpha)\tfrac{u}{|u|}$$

where e is a unit vector in the un-plane orthogonal to u (Fig. 3). Experimental measurements of c_l and c_d for a flat plate are reproduced in Fig. 4. From this plot, we notice that the following formulas provide a reasonable approximation for c_l and c_d:

$$c_l = \sin(2\alpha) \tag{3}$$

$$c_d = 2\sin^2(\alpha). \tag{4}$$

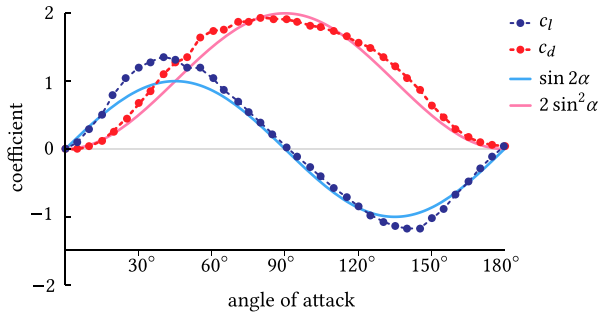

Fig. 4. The experimentally determined values of the lift and drag coefficients for a flat plate are reproduced here [Caplan and Gardner 2007, Fig. 6] and plotted alongside our trigonometric approximations (Eqns. 3 and 4).

The drag force acts in the direction opposite to the fluid flow ($-u/|u|$), and the lift force acts in a direction orthogonal to it (e). Therefore, the total force on the plate is

$$F = |F_l|\, e - |F_d|\, \tfrac{u}{|u|}. \tag{5}$$

Remarkably, this force admits a much simpler expression based on the approximations in Eqns. 3 and 4.

Proposition 1. *The lift and drag force on a flat plate is*

$$F = -\rho_f A|u|\langle u, n\rangle n.$$

Proof. Substituting $e = \frac{1}{\cos\alpha}(n + \sin\alpha\frac{u}{|u|})$ into Eqn. 5 yields

$$\begin{aligned} F &= |F_l|\, e - |F_d|\, \tfrac{u}{|u|} \\ &= \tfrac{1}{2}\rho_f A|u|^2\big(\sin(2\alpha)e - 2\sin^2(\alpha)\tfrac{u}{|u|}\big) \\ &= \tfrac{1}{2}\rho_f A|u|^2\big(2\sin\alpha(n + \sin\alpha\tfrac{u}{|u|}) - 2\sin^2(\alpha)\tfrac{u}{|u|}\big) \\ &= -\rho_f A|u|\langle u, n\rangle n. \end{aligned}$$

□

This gives us a parameter-free expression for the joint lift and drag forces experienced by a flat plate in a medium of given density.

Total force. If we treat the flat plate as a thin body made up of mesh elements on both sides of the plate, then we represent each portion of the plate twice, with different signs of n. Therefore, we take the total lift and drag force on a body B to be

$$F = -\tfrac{1}{2}\int_{\partial B} \rho_f |u|\langle u, n\rangle n\, dA, \tag{6}$$

which is summed over the mesh elements making up the surface ∂B of the body.

4.2 Added Mass in a Background Flow

We begin by generalizing the classical approach to added mass by incorporating the effects of a background flow before introducing a novel, local approximation which does not require a global solve on the fluid domain. Our approximation is obtained by estimating the kinetic energy of the fluid close to the body and calibrated to agree with the correct values on basic geometric primitives: spheres, cylinders, and flat plates. We validate our approach through examples of motions effected by accounting for the added mass.

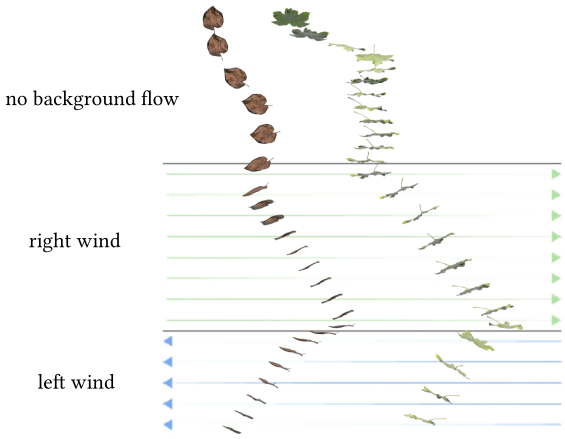

Fig. 5. The presence of a background flow enables easy modeling of leaves falling through the wind. (Video 1:19.)

Kirchhoff's tensor. Consider an incompressible fluid flowing with velocity $\mathbf{u}\colon \mathbb{R}^3 \to \mathbb{R}^3$ (Fig. 5). When a body B is immersed in the fluid with a certain initial velocity on its boundary the original velocity $\mathbf{u}$ has to be modified in order to make sure that the fluid does not penetrate the body. We will assume that the modified velocity field $\tilde{\mathbf{u}}$ is such that the L^2-norm of the difference $\tilde{\mathbf{u}} - \mathbf{u}$ is as small as possible. As a consequence of the Hodge decomposition, the perturbation of the fluid velocity field needs to be a gradient field and can be computed by solving a Poisson equation in the exterior volume of the body. To ensure feasibility, the initial body velocity must be volume-preserving. If it is not, the constant component of the Neumann data can be subtracted off.

Theorem 4.1. *Let $B \subset \mathbb{R}^3$ be a bounded domain with smooth boundary Σ and outward unit normal field n. Assume that the boundary points are moving with velocity $X\colon \Sigma \to \mathbb{R}^3$. Then among all divergence-free vector fields $\tilde{\mathbf{u}}\colon \overline{\mathbb{R}^3 \setminus B} \to \mathbb{R}^3$ that are compatible with the body motion, in the sense that $\langle \tilde{\mathbf{u}}, n\rangle = \langle X, n\rangle$ on Σ, the one that is closest in L^2-norm is $\tilde{\mathbf{u}} = \mathbf{u} + \operatorname{grad}\phi$ where ϕ is the solution of the Neumann problem*

$$\begin{cases} \Delta\phi = 0 & \text{in } \mathbb{R}^3 \setminus \overline{B}, \\ \langle \operatorname{grad}\phi, n\rangle = \langle X - \mathbf{u}, n\rangle & \text{on } \Sigma. \end{cases}$$

The kinetic energy of the fluid is therefore a function of the boundary velocity and the placement of the body in the fluid

$$E_{\text{fluid}} = \int_{\mathbb{R}^3\setminus B} \tfrac{1}{2}|\tilde{\mathbf{u}}|^2 \, \rho_f \, dx.$$

For an infinitesimal Euclidean motion $Y = (\omega, v) \in \mathfrak{se}(3)$ of a shape-changing body the velocity of the boundary points is given by

$$X(x) = Y(x) + X_\Sigma(x), \qquad Y(x) = \omega \times x + v$$

where $X_\Sigma\colon \Sigma \to \mathbb{R}^3$ is the component of the boundary velocity of the shape due to shape change.

The modified velocity field can hence be decomposed as

$$\tilde{\mathbf{u}} = \underbrace{\mathbf{u} + \operatorname{grad}\phi_{X_\Sigma} - \operatorname{grad}\phi_{\mathbf{u}}}_{\hat{\mathbf{u}}} + \operatorname{grad}\phi_Y,$$

where $\phi_{(\cdot)}$ denotes the solution of the Poisson equation with Neumann boundary data $\langle \cdot, n\rangle$. This yields the following decomposition of the kinetic energy of the fluid

$$\begin{aligned} E_{\text{fluid}} = &\int_{\mathbb{R}^3\setminus B} \tfrac{1}{2}|\operatorname{grad}\phi_Y|^2 \, \rho_f \, dx \\ &+ \int_{\mathbb{R}^3\setminus B} \langle \hat{\mathbf{u}}, \operatorname{grad}\phi_Y\rangle \, \rho_f \, dx \\ &+ \int_{\mathbb{R}^3\setminus B} \tfrac{1}{2}|\hat{\mathbf{u}}|^2 \, \rho_f \, dx. \end{aligned}$$

The first term is the kinetic energy of the potential flow induced by an infinitesimal Euclidean motion of the body (sans the shape change), and defines the Kirchhoff added mass tensor $\mathcal{I}_{\text{fluid}}\colon \mathfrak{se}(3) \to \mathfrak{se}(3)^*$ by

$$\tfrac{1}{2}\langle \mathcal{I}_{\text{fluid}} Y \mid Y\rangle = \int_{\mathbb{R}^3\setminus B} \tfrac{1}{2}|\operatorname{grad}\phi_Y|^2 \, \rho_f \, dx.$$

For rigid bodies in a quiescent fluid, this is the only nonzero term of E_{fluid}, and the resulting physical model has been studied in a number of different contexts [Kanso et al. 2005; Weißmann and Pinkall 2012].

For shape-changing bodies immersed in a nontrivial background flow, the kinetic energy of the fluid additionally contains a term that is linear in Y, that we will call $\mu_{\text{fluid}} = \mu_{\text{fluid}}(\mathbf{u}, X_\Sigma) \in \mathfrak{se}(3)^*$, and a constant term $E^0_{\text{fluid}} = E^0_{\text{fluid}}(\mathbf{u}, X_\Sigma)$:

$$E_{\text{fluid}} = \tfrac{1}{2}\langle \mathcal{I}_{\text{fluid}} Y \mid Y\rangle + \langle \mu_{\text{fluid}} \mid Y\rangle + E^0_{\text{fluid}} \tag{7}$$

where $\mu_{\text{fluid}} \in \mathfrak{se}(3)^*$ is defined by

$$\langle \mu_{\text{fluid}} \mid Y\rangle = \int_{\mathbb{R}^3\setminus B} \langle \hat{\mathbf{u}}, \operatorname{grad}\phi_Y\rangle \, \rho_f \, dx,$$

and

$$E^0_{\text{fluid}} = \int_{\mathbb{R}^3\setminus B} \tfrac{1}{2}|\hat{\mathbf{u}}|^2 \, \rho_f \, dx.$$

Eqn. 7 thus generalizes the concept of added mass to the setting with background flow.

The added mass tensor $\mathcal{I}_{\text{fluid}}$ depends on the body geometry only and can be computed before any simulation commences. However, μ_{fluid} and E^0_{fluid} also depend on the placement of the body inside the fluid, requiring their computation (solution of a potential problem) at each time step. To alleviate this computational burden, we now describe a local and explicit approximation that allows the kinetic energy of the fluid to be approximated very cheaply making it suitable for a fast rigid-body dynamics simulation.

Estimation of fluid kinetic energy. We approximate the kinetic energy of the fluid by the kinetic energy of the fluid near the boundary:

$$E_{\text{fluid}} \approx \int_\Sigma \tfrac{1}{2}|\tilde{\mathbf{u}}|^2 \, \rho_f \, \widetilde{dV}_\Sigma \geq \int_\Sigma \tfrac{1}{2}\langle \tilde{\mathbf{u}}, n\rangle^2 \, \rho_f \, \widetilde{dV}_\Sigma \tag{8}$$

where $\widetilde{dV}_\Sigma$ is a measure of external volume associated to the boundary. Since $\langle \tilde{\mathbf{u}}, n\rangle$ is just the Neumann data, Eqn. 8 yields an explicit approximation of the kinetic energy of the potential flow that does not require the solution of any partial differential equation:

$$\langle \mathcal{I}_{\text{fluid}} Y \mid Y\rangle \approx \int_\Sigma \langle \omega \times x + v, n\rangle^2 \, \rho_f \, \widetilde{dV}_\Sigma(x) \tag{9}$$

$$\langle \mu_{\text{fluid}} \mid Y\rangle \approx \int_\Sigma \langle \omega \times x + v, n\rangle \langle n, X_\Sigma\rangle \, \rho_f \, \widetilde{dV}_\Sigma(x). \tag{10}$$

Since $\langle \tilde{\mathbf{u}}, n\rangle = \langle X_\Sigma + Y, n\rangle$ does not depend on $\mathbf{u}$, our E_{fluid} approximation is independent of the background flow.

Volume on the boundary. To determine the measure of volume to associate with Σ, we take

$$\widetilde{dV}_\Sigma = \delta \, dA_\Sigma$$

where $\delta = \delta(\Sigma)$ is a coefficient (in units of m) which depends on the geometry of the body, and dA_Σ is the the area form of Σ. The coefficient δ can be thought of as describing the depth of influence of the boundary velocity on the fluid velocity in the region near the boundary. To determine an appropriate choice of this coefficient, we compare the added mass to the expected theoretical values on basic geometric primitives (Fig. 6).

The added mass tensor based on 3D potential flow can be computed explicitly for basic geometric shapes, by numerical simulation

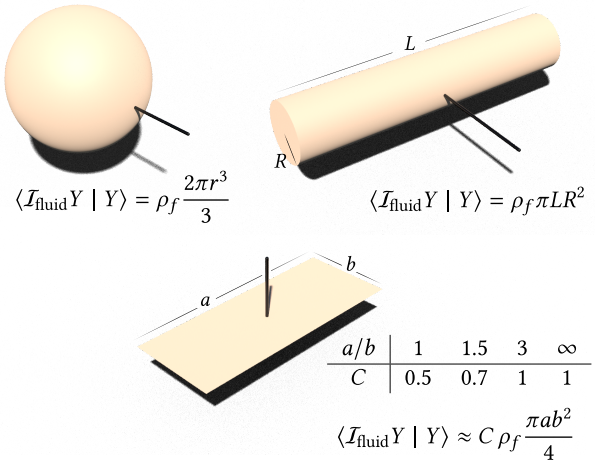

a/b	1	1.5	3	∞
C	0.5	0.7	1	1

Fig. 6. Diagonal values of the added mass computed via potential flow. For spheres and cylinders, we have exact expressions while for a plate the added mass is an approximation that depends on the aspect ratio.

on arbitrary shapes and one can find tabulated values of the diagonal component in the literature [Brennen 2004, Ch. Added Mass]. Such a diagonal component corresponds to the kinetic energy of the potential flow induced by a translation of the body in a particular direction, *i.e.*, $\langle \mathcal{I}_{\text{fluid}} Y \mid Y \rangle$ for an infinitesimal translation $Y \in \mathfrak{se}(3)$. For the sphere it is given by the mass of half its displaced volume for any direction, while for a cylinder the component of the added mass tensor in the radial directions is equal to the mass of its displaced volume (Fig. 6). In general however there is no relationship between the added mass and the displaced volume. This is most clearly seen for a flat plate that has nonzero added mass in the normal direction, yet it encloses no volume. Moreover, the added mass for the rectangular plate depends on the aspect ratio. Since locally all flat plates are the same we see that the choice of δ must depend on the global geometry of the body. Suitable global invariants are given by the "Quermaß Integrals" [Schröder 2008]. For a solid body in $\mathbb{R}^3$ neither volume nor Euler characteristic are of interest leaving functions of the area and mean width (integral of mean curvature) as possible candidates for $\delta(\Sigma)$.

The mean width shape invariant has the right units. However, neither for spheres nor cylinders does it yield the correct values for the added mass. For a planar region, the total mean curvature is equal to π times its perimeter, *i.e.*, independent of the aspect ratio. (Here we assume a closed surface formed by two back to back rectangles.)

Since area has units of m^2 another candidate, and the one we propose, is the ratio of area to mean width, or, said differently the inverse of average mean curvature

$$\delta(\Sigma) = \frac{1}{2} \frac{\int_\Sigma dA_\Sigma}{\int_\Sigma H \, dA_\Sigma}. \tag{11}$$

It reproduces the exact result for spheres and cylinders (Table 1). Moreover, for flat plates the value of the added mass depends on the aspect ratio and is within a factor of two of the correct value even as the aspect ratio approaches infinity (Fig. 6 lower right).

5 EQUATIONS OF MOTION

To derive the equations of motion of our shape-changing body we employ the Hamilton-Pontryagin variational principle [Kharevych et al. 2006; Bou-Rabee and Marsden 2009]. It yields equations of motion in momentum space rather than in velocity space. The latter would lead to the appearance of the time derivative of the inertia tensor which may be difficult to estimate from a time discrete sequence of poses. To account for shape changes we need to consider a time-dependent Lagrangian as well as additional terms that account for the momentum-induced by the changing shape in the body-fixed frame.

Lagrangian. The Lagrangian of a body going with the flow is the total kinetic energy of the fluid body system. We use the Lagrangian

$$\mathcal{L} \colon \mathrm{SE}(3) \times \mathfrak{se}(3) \times \mathbb{R} \to \mathbb{R} \tag{12}$$

$$(g, Y, t) \mapsto E_{\text{body}} + E_{\text{fluid}} = \tfrac{1}{2} \langle \mathcal{K}_t Y \mid Y \rangle + \langle \mu_t^0 \mid Y \rangle + E_t^0. \tag{13}$$

Here $\mathcal{K}_t = \mathcal{I}_{\text{body}} + \mathcal{I}_{\text{fluid}}$ is the time-dependent Kirchhoff tensor summing the body inertia tensor and the added mass tensor, and $\mu_t^0 = \mu_{\text{body}} + \mu_{\text{fluid}}$ is the total momentum induced by the motion of the body in the body-fixed frame (Eqns. 10 and 15). The term $E_t^0 = E_{\text{body}}^0 + E_{\text{fluid}}^0$ is a constant in g and Y, and so it does not influence the dynamics.

Hamilton-Pontryagin principle. It states that a mechanical system traverses a path that extremizes the action integral

$$\int_{t_0}^{t_1} \mathcal{L}(g, Y, t) + \langle \mu \mid g^{-1} g' - Y \rangle \, dt$$

under arbitrary variations of $g_t \in \mathrm{SE}(3)$, $Y_t \in \mathfrak{se}(3)$ and $\mu_t \in \mathfrak{se}(3)^*$ vanishing at the endpoints. The first term is the Lagrangian of the system. The second term is the pairing of a Lagrange multiplier μ with the kinematic constraint $g^{-1} g' = Y$, ensuring that the group and velocity variables are coupled correctly. The Lagrange multiplier μ can also be interpreted as the momentum of the system.

Theorem 5.1 (proof in App. C). *The equations of motion are*

$$\begin{cases} \frac{d}{dt} g = gY, \\ \frac{d}{dt} \mu = \mathrm{ad}_Y^* \, \mu \\ \mu = \mathcal{K} Y + \mu^0. \end{cases}$$

The first equation is known as the reconstruction equation since it describes how to reconstruct the Euclidean motion from its velocity, and the second and third equation describe the conservation of linear and angular momentum, written in terms of the momentum of the shape changing body in the body-fixed frame. Standard rigid body dynamics are a special case of the equations of motion in the absence of an ambient fluid ($\rho_f = 0$) and shape changes ($\mu^0 = 0$).

External forces. Newton's second law states that the applied forces and torques are equal to the time derivative of momentum. So to include forces, we modify the momentum evolution equation to

$$\frac{d}{dt} \mu = \mathrm{ad}_Y^* \, \mu + F \tag{14}$$

Table 1. Approximation of the added mass obtained by the boundary integral from Eqn. 9. For spheres and cylinders $\delta(\Sigma)$ gives the exact missing factor while for plates it produces a multiple of the harmonic mean of a and b when the desired value is $\min(a, b)$. On the more complicated geometries from Fig. 2 the approximation remains within a factor of 2 of the ground truth.

	sphere	cylinder	plate	bunny	propeller	coin
$\delta(\Sigma)$	$r/2$	R	$ab/\pi(a+b)$	0.29	0.30	0.43
approximation	$2\pi r^3/3$	πLR^2	$2a^2b^2/\pi(a+b)$	0.26	2.20	1.34
ground truth	$2\pi r^3/3$	πLR^2	$C\pi ab^2/4$	0.24	1.80	0.97
approximation/ground truth	1	1	$\frac{8}{C\pi^2}\frac{a}{a+b}$	1.08	1.22	1.38

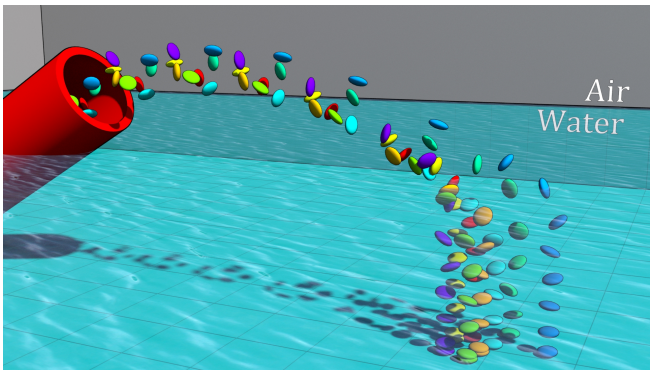

Fig. 7. Ellipses flying through air before sinking in water. This effect was achieved by updating the local fluid density ρ_f when a mesh element changes medium. (Video 0:37.)

where F describes the applied force and torque on the body in the body-fixed frame. Given an applied force and torque on the body in world space, described by an element $F_{\text{world}} \in \mathfrak{se}(3)^*$, we can transform it into the body-fixed frame by applying the group coadjoint action $F_{\text{body}} = \mathrm{Ad}^*_{g^{-1}} F_{\text{world}}$. In this way we inject lift and drag force (Prop. 1), gravity, buoyancy, and floor collision forces. In practice, any other external force can be included here as well.

6 NUMERICS

For the discrete time integration of our equations of motion (Thm. 5.1) we use a variational integrator based on a discrete Hamilton-Pontryagin principle which allows for stable integration with larger step sizes. The integrator is a simple generalization of [Bou-Rabee and Marsden 2009; Kobilarov et al. 2009], properly accounting for the varying inertia due to shape change.

6.1 Variational Integrator

The simplest choice of the discrete Hamilton-Pontryagin action sum that gives rise to a variational Euler integrator ([Bou-Rabee and Marsden 2009, page 214]) is

$$\sum_{k=0}^{N-1} h(\mathcal{L}(g_k, Y_{k+1}, t_k) + \langle\, \mu_{k+1} \mid \tfrac{1}{h}\tau^{-1}(g_k^{-1} g_{k+1}) - Y_{k+1} \,\rangle),$$

where h is the step size and $\tau\colon \mathfrak{se}(3) \to \mathrm{SE}(3)$ is a map from the Lie algebra to the group such as the Cayley or exponential map (App. B). Extremizing this action gives the discrete variational integrator we use and which is derived in App. C.2.

Algorithm 1 Variational Integrator

Input: shapes γ_k, γ_{k+1}; initial conditions g_k, Y_k, μ_k
Output: updated state $g_{k+1}, Y_{k+1}, \mu_{k+1}$; $\tilde{\gamma}_{k+1} = g_{k+1} \circ \gamma_{k+1}$

compute body inertia tensor $\mathcal{I}_{\text{body}}$ ▷ Alg. 3
compute momentum μ^0_{body} ▷ Alg. 4
compute added mass tensor $\mathcal{I}_{\text{fluid}}$ ▷ Alg. 5
compute fluid momentum μ^0_{fluid} ▷ Alg. 6
compute Kirchhoff tensor $\mathcal{K}_{t_k} \leftarrow \mathcal{I}_{\text{body}} + \mathcal{I}_{\text{fluid}}$
$\mu^0 \leftarrow \mu^0_{\text{body}} + \mu^0_{\text{fluid}}$
solve

$$(d\tau^{-1}_{-hY})^*(\mathcal{K}_{t_k} Y + \mu^0) = (d\tau^{-1}_{-hY_k})^* \mu_k + h\, F(g_k, Y, t_k)$$

for $Y \in \mathfrak{se}(3)$ by Newton's method
$Y_{k+1} \leftarrow Y$
$\mu_{k+1} \leftarrow \mathcal{K}_{t_k} Y_{k+1} + \mu^0_{t_k}$
$g_{k+1} \leftarrow g_k \tau(hY_{k+1})$

7 RESULTS

We have implemented our algorithm in SideFX' Houdini and achieve fast performance for all presented examples. We begin with experiments involving rigid bodies, focusing on effects due to the surrounding medium before dealing with shape-changing bodies.

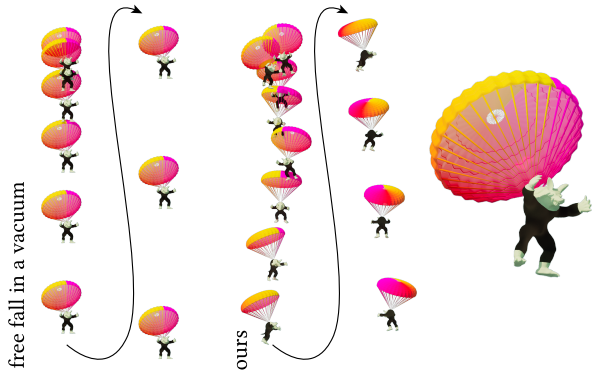

Fig. 8. *Left:* frames from free fall in a vacuum using regular rigid body dynamics. *Right:* after a brief acceleration phase the armadillo's descent reaches terminal velocity in our method since we account for the medium. (Video 0:54.)

7.1 Sinking in a Medium

[Weißmann and Pinkall 2012] computed the Kirchhoff tensor $\mathcal{K}$ by solving for potential fields with an integral equation formulation leading to dense linear systems. Our local approximation based on the inverse average mean curvature (Eqn. 11) achieves results equivalent to their experiments but at much lower computational cost. For the comparison we estimated the size of their objects with the aid of their video and set $\rho_f = 998.0\,\mathrm{kg/m^3}$ (water), $\rho_b = 1297.4\,\mathrm{kg/m^3}$ (silicone). A similar scenario is described by an object falling in air with the aid of a parachute (Fig. 8).

Using a local approximation of the fluid inertia we also support locally varying fluid density ρ_f, allowing objects to transition realistically between fluid media as shown in Fig. 7.

7.2 Fluttering and Autorotation

In most rigid body simulations air is neglected as a medium. However, light bodies can interact with air in very meaningful ways. One classic example is the fluttering fall of leaves. The large surface area results in significant added mass relative to their own weight, resulting in non-trivial deflections and rotations as shown in Figs. 9 and 5 (the latter showing additional background flow).

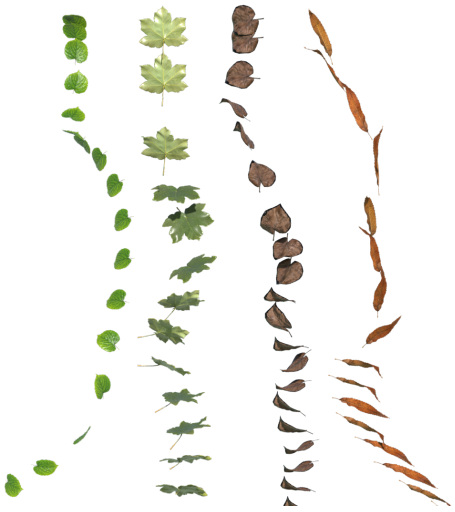

Fig. 9. Leaves falling in air. Their large surface area results in significant amounts of air mass being displaced relative to their weight, leading to deflections and rotations as they gain speed due to gravity. (Video 1:08.)

A special class of light objects falling in air autorotate. Maple seeds are typical examples of rotary seeds that reliably reduce their descent speed through rotation by virtue of their shape alone [Azuma and Yasuda 1989]. [Lee and Choi 2017] simulated such motion through full fluid simulation. We recover the same autorotating behavior with similar fall and rotation speed development without simulating the ambient fluid (see Fig. 10). To achieve this, the only parameter needed was the density of air $\rho_f = 1.225\,\mathrm{kg/m^3}$ together with an estimate of the mass distribution in the maple seed.

Similar to the maple seed, the paper copter is a simple model which also produces autorotation under gravity (Fig. 11). To reproduce

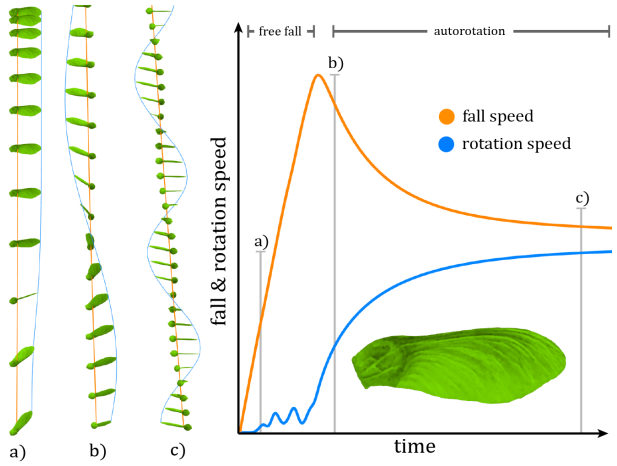

Fig. 10. Maple seeds are a typical example of rotary seeds [Azuma and Yasuda 1989]. Subject to gravity they glide to the ground while rotating. Left: Frames of a maple seed model transitioning from free fall to autorotation through our method. Right: the relative fall and rotation speed plotted over time approach a stable state. (Video 1:29.)

this we used the physical parameters of a paper model obtained from the *Exploratorium* (link). The piece of paper from which it was formed was 4 cm × 16 cm with a total mass of 500 mg. The paper clip weighed 1 g and the paper was 120 μm thick while the density of air was again set to $1.225\,\mathrm{kg/m^3}$.

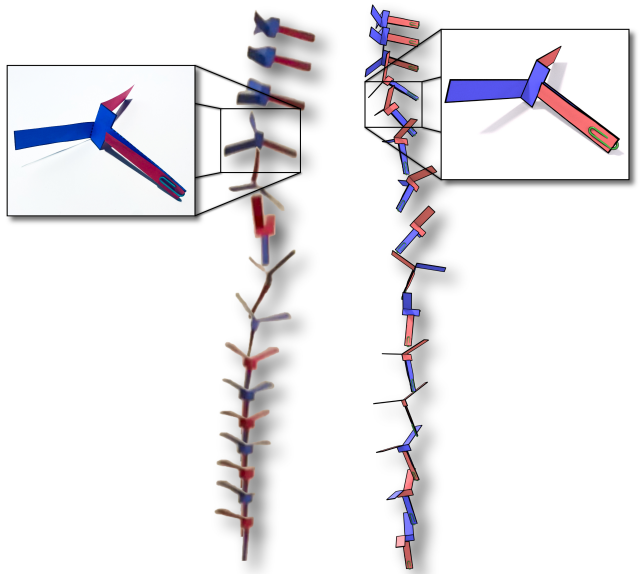

Fig. 11. Comparison of the flight of a paper copter. On the left frames from a video taken of an actual paper model (inset) falling. On the right our simulated model (inset) using the measurements and mass densities of the actual paper model as well as the correct value for air density. No other parameters needed specifying. (Video 2:16.)

7.3 Swimming and Flying through Shape Changes

Changing shapes while surrounded by an ambient fluid results in significant motion for the body, exemplified by the act of swimming. By inserting an animated sequence of shapes of a sea turtle and setting the ambient fluid density to be that of water, we recover its forward propulsion (Fig. 1, left). For the anguilliform locomotion of an eel in quiescent fluid we plot the forward momentum build-up due to its shape change and also observe how a terminal velocity is approached due to the increase in drag (Fig. 12). In both examples we assume the density of the swimmers to be that of water (998.0 kg/m^3).

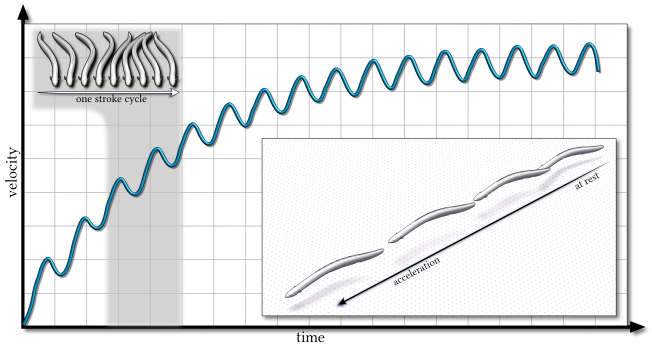

Fig. 12. An animated model of an eel swimming in quiescent water. We plot the forward velocity gained as a result of our algorithm. The insets display the eel animation and its movement in space. (Video 2:37.)

Another application of shape-changing bodies is the generation of forward propulsion through rotating propellers and steering through rudders. We animate a zeppelin to display both, which allows it to accelerate and turn through air as shown in Fig. 13.

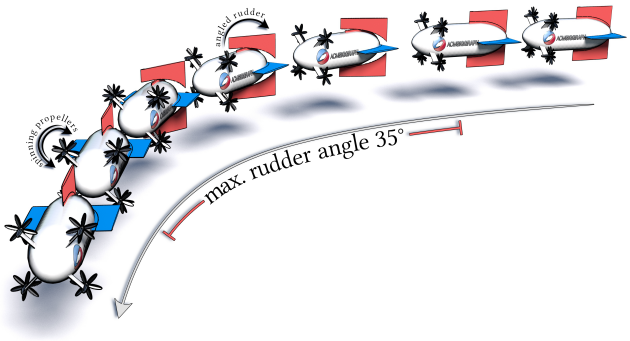

Fig. 13. A zeppelin is turned into a shape-changing body by rotating its propellers and rudders. The propellers result in forward momentum build up and the rudders deflect air for the zeppelin to turn. All without simulating the ambient fluid. (Video 2:49.)

7.4 Performance

We ran all computations on a Ryzen 7 5800X CPU and plotted the computation times of our variational integrator in Fig. 14 together with a performance study (red dots) of an ellipse discretized with increasing numbers of vertices. Each integration time step requires time linear in the number of vertices in the input geometry at approximately 30 milliseconds for every 1000 vertices. Thanks to the local approximation of the added mass tensor we introduced, the inertia tensor $\mathcal{K}$ is also computed in linear time and takes up approximately 5% of the total time per integration step. Note that it only needs recomputation when the body shape changes.

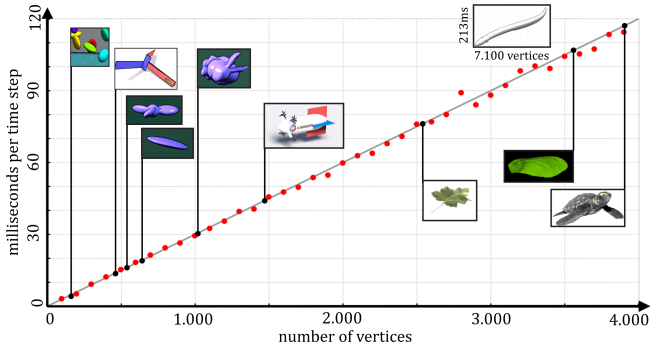

Fig. 14. A plot comparing the number of vertices in the input with the computation times per time step. Our algorithm displays linear complexity in the number of vertices. The insets indicate the performance of all our experiments. The red dots indicate the results of our performance study.

Our choice of time steps h varies between $1/400$ to $1/100$ depending on the situation. Our choice was determined by the speed of the obtained input animation (*e.g.*, turtle: $1/400$, eel: $1/200$), by the high speed of the phenomena (*e.g.*, maple seed & zeppelin's propellers: $1/200$) and by the stiffness of the floor collision constraint (*e.g.*, sinking in water: $1/300$). The number of vertices was chosen to be higher than necessary for visual fidelity, with one exception being the maple seed which would display issues entering autorotation when reducing the mesh resolution.

7.5 Limitations

In our algorithm we have made a number of approximations which impact the faithfulness of our simulations. For example, to incorporate the contribution of the surrounding fluid to the inertia of the body we proposed a local approximation instead of adding a suitable potential flow to the given background flow. The Kirchhoff added mass tensor also only considers the interaction of the object with fluid, ignoring any interactions between nearby objects and the surrounding environment. As it stands, our formula for the Kirchhoff tensor uses the inverse average mean curvature as a single global normalization factor. A possible refinement of our method in the future might be to decompose the body into a finite union of shapes (like in [Wei et al. 2022]) and use our formula to compute the contribution of the individual shapes to the added mass. On the whole, our approximations performed well in the experiments shown here. However, some phenomena could not be reproduced. Of the four distinct styles of trajectories of falling thin plates we were only able to reproduce two [Heisinger et al. 2014, Fig. 1 A & B] (falling and fluttering).

As is standard in the literature we have assumed the lift and drag forces to be proportional to the relative velocity squared. This implies modest Reynolds numbers while for lower Reynolds numbers a linear relationship, as used by Gross *et al.* [2023], is more correct. Ideally one would like to include a viscosity parameter.

Our approximations do not reproduce phenomena like the fact that a curved airplane wing produces more lift than a flat wing. Maybe a more detailed understanding of the role of vortex shedding in the generation of lift and drag could lead to a refined approximation that would account for these phenomena.

8 CONCLUSION

Given a set of poses of a body in an incompressible flow field, we determine its movement in space based on Newtonian mechanics. This setup generalizes ordinary rigid body simulation to settings with varying inertia, as prescribed by the given poses, and added mass as induced by movement in the surrounding medium. We introduced a novel local accounting of added mass which avoids the costly solution of repeated Poisson problems. Comparisons with experiments demonstrate that we can faithfully model motion effects due to lift and drag and added mass. Overall our approach enables the simulations of swimming sea turtles, flying zeppelins, leaves in wind, maple seed and paper copter autorotations in air, and objects falling in water, all without any fluid simulation and with linear complexity. Houdini source code to replicate examples is provided in the supplementary material.

In future work we hope to give a more detailed accounting of the momentum transfer between body and medium, in particular the shedding of vorticity and viscous effects such as skin friction.

ACKNOWLEDGMENTS

The bunny and armadillo mesh are courtesy of the Stanford Computer Graphics Laboratory. The eel and the turtle mesh are courtesy of DigitalLife3D at the University of Massachusetts, Amherst. We are grateful to *crowinhand* (link), *Zacxophone* (link), *bulut-* (link) and *FFishAsia* (link) for the models of the leaves. This work was supported in part by the Deutsche Forschungsgemeinschaft (DFG - German Research Foundation) - Project-ID 195170736 - TRR109 “Discretization in Geometry and Dynamics,” the Caltech Center for Information Science & Technology, and the Einstein Foundation Berlin. Additional support was provided by SideFX software.

REFERENCES

Akira Azuma and Kunio Yasuda. 1989. Flight Performance of Rotary Seeds. *J. Theor. Biol.* 138 (1989), 23–53.

Nawaf Bou-Rabee and Jerrold E Marsden. 2009. Hamilton–Pontryagin Integrators on Lie Groups Part I: Introduction and Structure-Preserving Properties. *Found. Comp. Math.* 9, 2 (2009), 197–219.

Christopher E. Brennen. 2004. *Internet Book on Fluid Dynamics.* Dankat Publishing, Chapter Values of the Added Mass.

Tyson Brochu, Todd Keeler, and Robert Bridson. 2012. Linear-Time Smoke Animation with Vortex Sheet Meshes. *Proc. Symp. Comp. Anim.* (2012), 87–95.

Nicholas Caplan and Trevor N. Gardner. 2007. A Fluid Dynamic Investigation of the Big Blade and Macon Oar Blade Designs in Rowing Propulsion. *J. Sports Sci.* 25, 6 (2007), 643–650.

Mark Carlson, Peter J. Mucha, and Greg Turk. 2004. Rigid Fluid: Animating the Interplay between Rigid Bodies and Fluid. *ACM Trans. Graph.* 23, 3 (2004), 377–384.

S. J. Corkery, H. Babinsky, and W. R. Graham. 2019. Quantification of Added-Mass Effects using Particle Image Velocimetry Data for a Translating and Rotating Flat Plate. *J. Fl. Mech.* 870 (2019), 492–518.

Anthony R. Dobrovolskis. 1996. Inertia of Any Polyhedron. *Icarus* 124, 2 (1996), 698–704.

Oliver Gross, Yousuf Soliman, Marcel Padilla, Felix Knöppel, Ulrich Pinkall, and Peter Schröder. 2023. Motion from Shape Change. *ACM Trans. Graph.* 42, 4 (2023), 107:1–11.

Luke Heisinger, Paul Newton, and Eva Kanso. 2014. Coins Falling in Water. *J. Fl. Mech.* 742 (2014), 243–253.

E. Ju, J. Won, J. Lee, B. Choi, J. Noh, and M. Gyu Choi. 2013. Data-Driven Control of Flapping Flight. *ACM Trans. Graph.* 32, 5 (2013), 151:1–12.

Eva Kanso, Jerrold E. Marsden, Clancy W. Rowley, and J. B. Melli-Huber. 2005. Locomotion of Articulated Bodies in a Perfect Fluid. *J. Non-L. Sci.* 15 (2005), 255–289.

Liliya Kharevych, Weiwei, Yiying Tong, Eva Kanso, Jerrold Marsden, Peter Schröder, and Mathieu Desbrun. 2006. Geometric, Variational Integrators for Computer Animation. In *Proc. Symp. Comp. Anim.* Eurographics Ass., 43–51.

Gustav Kirchhoff. 1870. Ueber die Bewegung eines Rotationskörpers in einer Flüssigkeit. *J. Reine Angew. Math.* 1870, 71 (1870), 237–262.

Gustav Kirchhoff. 1876. *Vorlesungen über mathematische Physik.* Teubner, 233–250.

Marin Kobilarov, Keenan Crane, and Mathieu Desbrun. 2009. Lie Group Integrators for Animation and Control of Vehicles. *ACM Trans. Graph.* 28, 2 (2009), 16:1–14.

Injae Lee and Haecheon Choi. 2017. Flight of a Falling Maple Seed. *Phys. R. Fl.* 2, 9 (2017), 090511:1–3.

Michael Lentine, Jon Tomas Gretarsson, Craig Schroeder, Avi Robinson-Mosher, and Ronald Fedkiw. 2011. Creature Control in a Fluid Environment. *IEEE Trans. Vis. Comp. Graph.* 17, 5 (2011), 682–693.

Eric Limacher, Chris Morton, and David Wood. 2018. Generalized Derivation of the Added-Mass and Circulatory Forces for Viscous Flow. *Phys. R. Fl.* 3, 1 (2018), 014701:1–25.

Eric Limacher, Chris Morton, and David Wood. 2019. On the Calculation of Force from PIV Data Using the Generalized Added-Mass and Cirulatory Force Decomposition. *Exp. in Fl.* 60, 4 (2019), 1–22.

Sehee Min, Jungdam Won, Seunghwan Lee, Jungnam Park, and Jehee Lee. 2019. SoftCon: Simulation and Control of Soft-Bodied Animals with Biomimetic Actuators. *ACM Trans. Graph.* 38, 6 (2019), 208:1–12.

Andreas Müller. 2021. Review of the exponential and Cayley map on SE (3) as relevant for Lie group integration of the generalized Poisson equation and flexible multibody systems. *Proc. Roy. Soc. A* 477, 2253 (2021), 20210303.

Oktar Ozgen, Marcelo Kallmann, Lynnette Es Ramirez, and Carlos Fm Coimbra. 2010. Underwater Cloth Simulation with Fractional Derivatives. *ACM Trans. Graph.* 29, 3 (2010), 23:1–9.

M. Piñeirua, R. Godoy-Diana, and B. Thiria. 2015. Resistive Thrust Production can be as crucial as Added Mass Mechanisms for Inertial Undulatory Swimmers. *Phys. R. E* 92, 2 (2015), 021001:1–6.

Peter Schröder. 2008. What can we Measure? In *Discrete Differential Geometry*, Alexander I. Bobenko, Peter Schröder, John M. Sullivan, and Günther M. Ziegler (Eds.). Oberwolfach Seminars, Vol. 38. Birkhäuser Verlag.

Jie Tan, Yuting Gu, Greg Turk, and C. Karen Liu. 2011. Articulated Swimming Creatures. *ACM Trans. Graph.* 30, 4 (2011), 58:1–12.

Xiaoyuan Tu and Demetri Terzopoulos. 1994. Artificial Fishes: Physics, Locomotion, Perception, Behavior. In *Proc. ACM/SIGGRAPH Conf.* 43–50.

Xinyue Wei, Minghua Liu, Zhan Ling, and Hao Su. 2022. Approximate convex decomposition for 3D meshes with collision-aware concavity and tree search. *ACM Trans. Graph.* 41, 4, Article 42 (jul 2022), 18 pages. https://doi.org/10.1145/3528223.3530103

Steffen Weißmann and Ulrich Pinkall. 2012. Underwater Rigid Body Dynamics. *ACM Trans. Graph.* 31, 4 (2012), 104:1–7.

Jakub Wejchert and David Haumann. 1991. Animation Aerodynamics. In *Comp. Graph. (Proc. of ACM/SIGGRAPH Conf.)*, Vol. 25. 19–22.

Jia-Chi Wu and Zoran Popović. 2003. Realistic Modeling of Bird Flight Animations. *ACM Trans. Graph.* 22, 3 (2003), 888–895.

A INERTIA AND MOMENTUM ON SE(3)

Matrix representations of the body and fluid inertia tensors are needed for implementation. Identifying $\mathfrak{se}(3)$ and $\mathfrak{se}(3)^*$ with $\mathbb{R}^6$ we can treat the inertia tensors as 6×6 matrices.

For $x \in \mathbb{R}^3$, let $(x\times) \in \mathbb{R}^{3\times3}$ denote the skew-symmetric cross product matrix satisfying $(x\times)y = x \times y$ for all $y \in \mathbb{R}^3$, and let $\mathrm{id}_{\mathbb{R}^3} \in \mathbb{R}^{3\times3}$ denote the identity matrix.

Decompose the body inertia tensor $\mathcal{I}_{\mathrm{body}} \in \mathbb{R}^{6\times6}$ and added mass tensor $\mathcal{I}_{\mathrm{fluid}} \in \mathbb{R}^{6\times6}$ as

$$\mathcal{I}_{\mathrm{body}} = \begin{pmatrix} I^b_{\omega,\omega} & I^b_{\omega,v} \\ I^b_{v,\omega} & I^b_{v,v} \end{pmatrix}, \qquad \mathcal{I}_{\mathrm{fluid}} = \begin{pmatrix} I^f_{\omega,\omega} & I^f_{\omega,v} \\ I^f_{v,\omega} & I^f_{v,v} \end{pmatrix}.$$

Then Eqn. 2 yields the body kinetic energy with

$$I^b_{\omega,\omega} = \int_B (\gamma\times)^\top(\gamma\times)\ \rho_b\ dx, \qquad I^b_{\omega,v} = \int_B (\gamma\times)\ \rho_b\ dx,$$
$$I^b_{v,\omega} = \int_B (\gamma\times)^\top\ \rho_b\ dx, \qquad I^b_{v,v} = \int_B \mathrm{id}_{\mathbb{R}^3}\ \rho_b\ dx.$$

The momentum $\mu_{\text{body}} = (l^b, p^b)$ of γ is

$$l^b = \int_B \gamma\times\gamma'\ \rho_b\ dx, \qquad p^b = \int_B \gamma'\ \rho_b\ dx. \tag{15}$$

The approximation described in Eqn. 9 is obtained by taking

$$I^f_{\omega,\omega} = \int_\Sigma (\gamma\times n)\otimes(\gamma\times n)\ \widetilde{dV}_\Sigma, \quad I^f_{\omega,v} = \int_\Sigma (\gamma\times n)\otimes n\ \widetilde{dV}_\Sigma,$$
$$I^f_{v,\omega} = \int_\Sigma n\otimes(\gamma\times n)\ \widetilde{dV}_\Sigma, \qquad I^f_{v,v} = \int_\Sigma n\otimes n\ \widetilde{dV}_\Sigma.$$

The corresponding momentum approximation $\mu_{\text{fluid}} = (l^f, p^f)$ described in Eqn. 10 is given by

$$l^f = \int_\Sigma \langle\gamma', n\rangle(\gamma\times n)\ \widetilde{dV}_\Sigma, \qquad p^f = \int_\Sigma \langle\gamma', n\rangle n\ \widetilde{dV}_\Sigma. \tag{16}$$

B CAYLEY MAP

The numerical integration of the equations of motion is done with the help of the Cayley map, which we denote by $\tau\colon \mathfrak{se}(3) \to \mathrm{SE}(3)$. The Cayley map is a well-known approximation of the exponential map and can be explicitly written as

$$\tau(Y) = \left(\mathrm{id}_{\mathbb{R}^3} + \tfrac{4}{4+|\omega|^2}((\omega\times) + \tfrac{1}{2}(\omega\times)^2),\ \tfrac{2}{4+|\omega|^2}(2v + \omega\times v)\right)$$

for $Y = (\omega, v) \in \mathfrak{se}(3)$ [Müller 2021, Eqn. 3.14]. The first entry describes the rotational component of the resulting Euclidean motion and the second entry the translational component. Alternative variational integrators can be derived by taking τ to be the exponential map.

The differential of τ^{-1} also shows up in the discrete equations of motion. To deal with it efficiently, we use the inverse right-trivialized differential $d\tau^{-1}\colon \mathfrak{se}(3)\times\mathfrak{se}(3) \to \mathfrak{se}(3)$ [Müller 2021, Eqn. 3.17]. It is linear in its second argument, and so under the identification of $\mathfrak{se}(3)$ with $\mathbb{R}^6$ it is identified with a (6×6)-matrix. Explicitly,

$$d\tau^{-1}_Y = \begin{pmatrix} \mathrm{id}_{\mathbb{R}^3} - \frac{1}{2}(\omega\times) + \frac{1}{4}\omega\otimes\omega & 0 \\ -\frac{1}{2}((v\times) - \frac{1}{2}(\omega\times)(v\times)) & \mathrm{id}_{\mathbb{R}^3} - \frac{1}{2}(\omega\times) \end{pmatrix}. \tag{17}$$

B.1 Pseudocode

Throughout this section we let $M = (V, E, F)$ be a triangle mesh describing the boundary of the body. The following notation will simplify some of the expressions that follow: for a function $\gamma\colon V \to \mathbb{R}^3$ defined on the vertices of M, we will denote its linear interpolation to the barycenter of a triangle ijk by $\gamma_{ijk} \coloneqq \frac{1}{3}(\gamma_i + \gamma_j + \gamma_k)$.

Below, we provide pseudocode to compute the Kirchhoff tensor and momentum needed for the integration of the equations of motion. We describe how to compute the body inertia tensor and momentum in the case when the mass is concentrated on the vertices of V. The inertia tensor of a body with uniform mass distribution in a volume can also be computed as a surface integral [Dobrovolskis 1996], and can be used as a swap-in replacement for $\mathcal{I}_{\text{body}}$ in the algorithm.

Algorithm 2 Lift and Drag Forces

Input: vertex positions $\gamma\colon V \to \mathbb{R}^3$; velocities $v\colon V \to \mathbb{R}^3$; background flow $\mathbf{u}\colon \mathbb{R}^3 \to \mathbb{R}^3$
Output: total force and torque due to lift and drag $F \in \mathbb{R}^6$

compute face areas $A\colon F \to \mathbb{R}_{\geq 0}$
compute face normals $n\colon F \to \mathbb{R}_{\geq 0}$
$u \leftarrow v - \mathbf{u}\circ\gamma$ ▷ relative velocities
$\tau \leftarrow \rho_f \sum_{ijk\in F} |u_{ijk}|\langle u_{ijk}, n_{ijk}\rangle(\gamma_{ijk}\times n_{ijk})A_{ijk}$
$f \leftarrow \rho_f \sum_{ijk\in F} |u_{ijk}|\langle u_{ijk}, n_{ijk}\rangle n_{ijk}$
$F \leftarrow (\tau, f)$

Algorithm 3 Body Inertia Tensor

Input: vertex positions $\gamma\colon V \to \mathbb{R}^3$; mass density $\rho_b\colon V \to \mathbb{R}_{\geq 0}$
Output: body inertia tensor $\mathcal{I}_{\text{body}} \in \mathbb{R}^{6\times 6}$

$I^b_{\omega,\omega} \leftarrow \sum_{i\in V}(\gamma_i\times)^\top(\gamma_i\times)(\rho_b)_i$
$I^b_{\omega,v} \leftarrow \sum_{i\in V}(\gamma_i\times)(\rho_b)_i$
$I^b_{v,v} \leftarrow \sum_{i\in V}(\rho_b)_i\,\mathrm{id}_{\mathbb{R}^3}$
$\mathcal{I}_{\text{body}} \leftarrow \begin{pmatrix} I^b_{\omega,\omega} & I^b_{\omega,v} \\ (I^b_{\omega,v})^\top & I^b_{v,v} \end{pmatrix}$

Algorithm 4 Body Momentum

Input: vertex positions $\gamma_k, \gamma_{k+1}\colon V \to \mathbb{R}^3$; mass density $\rho_b\colon V \to \mathbb{R}_{\geq 0}$
Output: body momentum $\mu^0_{\text{body}} \in \mathbb{R}^6$

$\gamma' \leftarrow (\gamma_{k+1} - \gamma_k)/h$
$l^b \leftarrow \sum_{i\in V}\gamma_i\times\gamma'_i\ (\rho_b)_i$
$p^b \leftarrow \sum_{i\in V}\gamma'_i\ (\rho_b)_i$
$\mu^0_{\text{body}} \leftarrow (l^b, p^b)^\top$

Algorithm 5 Added Mass Tensor

Input: vertex positions $\gamma\colon V \to \mathbb{R}^3$
Output: added mass tensor $\mathcal{I}_{\text{fluid}} \in \mathbb{R}^{6\times 6}$

compute face areas $A\colon F \to \mathbb{R}_{\geq 0}$
compute face normals $n\colon F \to S^2$
compute bending angles $\alpha\colon E \to [-\pi, \pi]$
compute edge lengths $\ell\colon E \to \mathbb{R}_{\geq 0}$
$\delta \leftarrow (\sum_{ijk\in F} A_{ijk})/(\sum_{ij\in E}\alpha_{ij}\ell_{ij})$
$I^f_{\omega,\omega} \leftarrow \rho_f\delta\sum_{ijk\in F}(\gamma_{ijk}\times n_{ijk})\otimes(\gamma_{ijk}\times n_{ijk})\,A_{ijk}$
$I^f_{\omega,v} \leftarrow \rho_f\delta\sum_{ijk\in F}(\gamma_{ijk}\times n_{ijk})\otimes n_{ijk}\,A_{ijk}$
$I^f_{v,v} \leftarrow \rho_f\delta\sum_{ijk\in F} n_{ijk}\otimes n_{ijk}\,A_{ijk}$
$\mathcal{I}_{\text{fluid}} \leftarrow \begin{pmatrix} I^f_{\omega,\omega} & I^f_{\omega,v} \\ (I^f_{\omega,v})^\top & I^f_{v,v} \end{pmatrix}$

C HAMILTON-PONTRYAGIN WITH TIME-VARYING LAGRANGIANS

Here we derive the equations of motion in both the continuous and discrete setting according to the Hamilton-Pontryagin principle. The derivation is standard for autonomous Lagrangians [Bou-Rabee

Algorithm 6 Fluid Momentum

Input: vertex positions $\gamma_k, \gamma_{k+1} \colon V \to \mathbb{R}^3$
Output: fluid momentum $\mu^0_{\text{fluid}} \in \mathbb{R}^6$

compute face areas $A \colon F \to \mathbb{R}_{\geq 0}$
compute face normals $n \colon F \to \mathbb{R}_{\geq 0}$
compute δ from Alg. 5
$\gamma' \leftarrow (\gamma_{k+1} - \gamma_k)/h$
$l^f \leftarrow \rho_f \delta \sum_{ijk \in F} \langle \gamma'_{ijk}, n_{ijk} \rangle (\gamma_{ijk} \times n_{ijk})\, A_{ijk}$
$p^f \leftarrow \rho_f \delta \sum_{ijk \in F} \langle \gamma'_{ijk}, n_{ijk} \rangle n_{ijk}\, A_{ijk}$
$\mu^0_{\text{fluid}} \leftarrow (l^f, p^f)^\top$

and Marsden 2009]. As the Euler-Lagrange equations do not change whether a Lagrangian is time-dependent or not the continuous equations of motion are the same as in the autonomous setting.

C.1 Continuous Equations of Motion

Consider a Lie group G with Lie algebra $\mathfrak{g}$ and a Lagrangian $\mathcal{L} \colon G \times \mathfrak{g} \times \mathbb{R} \to \mathbb{R}$. The Hamilton-Pontryagin action is

$$\mathrm{HP} = \int_{t_0}^{t_1} \mathcal{L}(g, Y, t) + \langle\, \mu \mid g^{-1} g' - Y \,\rangle \, dt.$$

Theorem C.1. *The equations of motion are*

$$\begin{cases} \frac{d}{dt} g = gY, \\ \frac{d}{dt} \mu = \mathrm{ad}^*_Y \mu + g \frac{\partial \mathcal{L}}{\partial g} \\ \mu = \frac{\partial \mathcal{L}}{\partial Y} \end{cases}$$

Proof. Variations of HP with respect to μ

$$\mathring{\mathrm{HP}} = \int_{t_0}^{t_1} \langle\, \mathring{\mu} \mid g^{-1} g' - Y \,\rangle \, dt.$$

give rise to the reconstruction equation $\frac{d}{dt} g = gY$. Variations of HP with respect to Y

$$\mathring{\mathrm{HP}} = \int_{t_0}^{t_1} \langle\, \frac{\partial \mathcal{L}}{\partial Y} - \mu \mid \mathring{Y} \,\rangle \, dt$$

give rise to $\mu = \frac{\partial \mathcal{L}}{\partial Y}$. To compute variations of HP with respect to g we introduce $\mathring{\eta} = g^{-1} \mathring{g}$

$$\mathring{\mathrm{HP}} = \int_{t_0}^{t_1} \langle\, g \frac{\partial \mathcal{L}}{\partial Y} \mid \mathring{\eta} \,\rangle + \langle\, \mu \mid \mathring{\eta}' + \mathrm{ad}_Y \mathring{\eta} \,\rangle \, dt,$$

where we used that $\mathring{\eta}' + \mathrm{ad}_Y \mathring{\eta} = (g^{-1} g')^\circ$. Integration by parts now yields the momentum evolution equation $\frac{d}{dt} \mu = \mathrm{ad}^*_Y \mu + g \frac{\partial \mathcal{L}}{\partial g}$. □

The momentum evolution equation contains an additional term $g \frac{\partial L}{\partial g}$ that only shows up, if, in the presence of a background flow, the added mass is computed via potential theory. However, our local approximation of the added mass does not depend on g and so this term is zero for the case that we are interested in integrating (*cf.*, Thm. 5.1).

C.2 Discrete Equations of Motions

To discretize the kinematic constraint $g^{-1} g' - Y$ we use a local diffeomorphism $\tau \colon \mathfrak{g} \to G$ like the exponential or Cayley map. Partition the time-interval $[0, T]$ into N steps of size h: $\{0 = t_0, \ldots, t_{N-1} = T\}$ indexed by k. The discrete Hamilton-Pontryagin action sum

$$\begin{aligned} \mathrm{HP} \colon & G^N \times \mathfrak{g}^N \times (\mathfrak{g}^*)^N \to \mathbb{R} \\ & (\{g_k\}, \{Y_k\}, \{\mu_k\}) \mapsto \sum_{k=0}^{N-1} h\big(\mathcal{L}(g_k, Y_{k+1}, t_k) \\ & \qquad + \langle \mu_{k+1} \mid \tfrac{1}{h} \tau^{-1}(g_k^{-1} g_{k+1}) - Y_{k+1} \rangle\big) \end{aligned}$$

gives rise to a variational backwards Euler integrator. To incorporate external forces $F \colon G \times \mathfrak{g} \times \mathbb{R} \to \mathbb{R}$ we discretize the virtual work:

$$\mathcal{F} = \sum_{k=0}^{N-1} h \langle F(g_k, Y_{k+1}, t_k) \mid g_k^{-1} \mathring{g}_k \rangle.$$

Theorem C.2. *The discrete equations of motion determine* $(g_{k+1}, Y_{k+1}, \mu_{k+1})$ *from* (g_k, Y_k, μ_k) *as the solution to*

$$\begin{cases} g_{k+1} = g_k \tau(h Y_{k+1}) \\ (d\tau^{-1}_{hY_{k+1}})^* \mu_{k+1} - (d\tau^{-1}_{-hY_k})^* \mu_k = h\big(g_k \frac{\partial \mathcal{L}}{\partial g}(g_k, Y_{k+1}, t_k) \\ \qquad\qquad + F(g_k, Y_{k+1}, t_k)\big) \\ \mu_{k+1} = \frac{\partial \mathcal{L}}{\partial Y}(g_k, Y_{k+1}, t_k) \end{cases}$$

Proof. Variations of HP with respect to μ

$$\mathring{\mathrm{HP}} = \sum_{k=0}^{N-1} \langle \mathring{\mu}_{k+1} \mid \tfrac{1}{h} \tau^{-1}(g_k^{-1} g_{k+1}) - Y_{k+1} \rangle$$

give rise to the reconstruction equation $g_{k+1} = g_k \tau(h Y_{k+1})$. Variations of HP with respect to Y

$$\mathring{\mathrm{HP}} = \sum_{k=0}^{N-1} \langle \frac{\partial \mathcal{L}}{\partial Y}(g_k, Y_{k+1}, t_k) - \mu_{k+1} \mid \mathring{Y}_{k+1} \rangle$$

give rise to $\mu_{k+1} = \frac{\partial \mathcal{L}}{\partial Y}(g_k, Y_{k+1}, t_k)$. To compute variations of HP with respect to g we introduce $\mathring{\eta}_k = g_k^{-1} \mathring{g}_k$

$$\begin{aligned} \mathring{\mathrm{HP}} = & \sum_{k=0}^{N-1} \langle g_k \frac{\partial \mathcal{L}}{\partial g}(g_k, Y_{k+1}, t_k) \mid \mathring{\eta}_k \rangle \\ & + \sum_{k=0}^{N-1} \langle \mu_{k+1} \mid -\tfrac{1}{h} d\tau^{-1}_{hY_{k+1}}(\mathring{\eta}_k) + \tfrac{1}{h} d\tau^{-1}_{-hY_{k+1}}(\mathring{\eta}_{k+1}) \rangle, \end{aligned}$$

where we used the definition of the right-trivialized differential to compute the derivative of the kinematic constraint. Rearranging the sum to isolate the pairing with $\mathring{\eta}_k$ yields

$$\mathring{\mathrm{HP}} = \sum_{k=0}^{N-1} \langle g_k \frac{\partial \mathcal{L}}{\partial g}(g_k, Y_{k+1}, t_k) - \tfrac{1}{h} (d\tau^{-1}_{hY_{k+1}})^* \mu_{k+1} + \tfrac{1}{h} (d\tau^{-1}_{-hY_k})^* \mu_k \mid \mathring{\eta}_k \rangle.$$

The momentum evolution equation then follows from the balance between the variation of HP with respect to g and the virtual work done by the external forces:

$$(d\tau^{-1}_{hY_{k+1}})^* \mu_{k+1} - (d\tau^{-1}_{-hY_k})^* \mu_k = h(g_k \frac{\partial \mathcal{L}}{\partial g}(g_k, Y_{k+1}, t_k) + F(g_k, Y_{k+1}, t_k)).$$

□